Magnetic field dependence of the density of states in the multiband superconductor β-Bi_2Pd

E. Herrera,[1] I. Guillamón,[1,2] J. A. Galvis,[1,3] A. Correa,[4] A. Fente,[1] R. F. Luccas,[4] F. J. Mompean,[2,4] M. García-Hernández,[2,4] S. Vieira,[1,2] J. P. Brison,[5,6] and H. Suderow[1,2,*]

[1]*Laboratorio de Bajas Temperaturas, Departamento de Física de la Materia Condensada, Instituto Nicolás Cabrera and Condensed Matter Physics Center (IFIMAC), Universidad Autónoma de Madrid, E-28049 Madrid, Spain*

[2]*Unidad Asociada de Bajas Temperaturas y Altos Campos Magnéticos, UAM, CSIC, E-28049 Madrid, Spain*

[3]*Departamento de Ciencias Naturales, Facultad de Ingeniera, Universidad Central, 110311 Bogotá, Colombia*

[4]*Instituto de Ciencia de Materiales de Madrid, Consejo Superior de Investigaciones Científicas (ICMM-CSIC), Sor Juana Inés de la Cruz 3, 28049 Madrid, Spain*

[5]*Université Grenoble Alpes, INAC-SPSMS, F-38000 Grenoble, France*

[6]*CEA, INAC-SPSMS D-38000 Grenoble, France*

(Received 14 January 2015; revised manuscript received 3 June 2015; published 17 August 2015)

We present very low-temperature scanning tunneling microscopy (STM) experiments on single-crystalline samples of the superconductor β-Bi_2Pd. We find a single superconducting gap from the zero-field tunneling conductance. However, the magnetic field dependence of the intervortex tunneling conductance is higher than the one expected in a single-gap superconductor. Such an increase in the intervortex tunneling conductance has been found in superconductors with multiple superconducting gaps. We also find that the hexagonal vortex lattice is locked to the square atomic lattice as expected in crystalline superconductors with anisotropic Fermi surfaces. Moreover, we compare the upper critical field $H_{c2}(T)$ obtained in our sample with previous measurements and find that $H_{c2}(T)$ does not increase by reducing the mean free path. We fit $H_{c2}(T)$ and show that multiband Fermi surface is needed to explain the observed behavior. We propose that β-Bi_2Pd is a single-gap multiband superconductor. We anticipate that single-gap superconductivity might often occur in compounds with anisotropic multiband Fermi surfaces.

DOI: 10.1103/PhysRevB.92.054507 PACS number(s): 74.55.+v, 74.20.Fg, 74.25.Uv, 74.70.Ad

I. INTRODUCTION

Superconductivity is often found in binary metallic compounds with critical temperatures of the order of liquid helium temperature. Some are reviewed in Ref. [1] and give type-II superconductors. Among them, MgB_2 is peculiar, with a critical temperature $T_c = 40$ K unsurpassed by related binary compounds. Such a high-T_c results from the combination of the strong electron-phonon coupling of the two-dimensional σ bands and weak interband mixing with the three-dimensional π bands [2–8]. Each set of bands is derived from orthogonal orbital wave functions, leading to two well defined superconducting gap features. Multigap and multiband superconductivity have been conceptually linked together since the discovery of MgB_2, suggesting that materials showing different Fermi surface sheets also have different superconducting gaps in each sheet.

Under magnetic fields, vortex core overlap is governed by the Fermi surface velocity (see Refs. [9–11]). In MgB_2, enhanced vortex core overlap has been observed and related to the Fermi surface properties of the sheet having a smaller sized superconducting gap [8,12–14]. This leads to a strong increase of the density of intervortex quasiparticle excitations measured by scanning tunneling microscopy and spectroscopy (STM) [12,13], and of the overall density of states measured by specific heat or thermal conductivity, when applying a magnetic field. The upper critical field shows a positive curvature, instead of the negative curvature expected within single-gap s-wave BCS superconductivity [10,15–22]. The same occurs in many different compounds, including heavy fermions, borocarbides, and Fe-based superconductors [11,23–29]. So far, the increased density of states and positive curvature of H_{c2} close to T_c have been explained through multigap superconductivity. However, the detailed mixed phase properties of a single-gap s-wave superconductor and the influence of multiband and of anisotropic Fermi surfaces in the mixed phase remain unclear.

Here, we show how superconducting features are modified by a multiband Fermi surface. We measure β-Bi_2Pd ($T_c = 5$ K [17,30]) with a very low-temperature STM. Our sample is moderately in the dirty limit (mean free path ℓ smaller than superconducting coherence length ξ, $\ell < \xi$) and the Fermi surface shows multiple sheets of mixed orbital character [17,31,32]. The situation is opposed to MgB_2, with σ and π sheets that remain well separated even in presence of defects [10]. At 150 mK, we obtain atomic scale imaging and the hexagonal vortex lattice. At zero field, we find single-gap behavior following s-wave BCS theory but observe multiband properties in the mixed phase. The density of states in-between vortices increases more than expected for an isotropic single-gap superconductor and the hexagonal vortex lattice locks to the square crystal lattice.

II. CRYSTAL GROWTH AND EXPERIMENTAL METHODS

Single crystals of β-Bi_2Pd were grown using slight excess of Bi [33,34]. We grew our samples from high-purity Bi (Alfa Aesar 99.99%) and Pd (Alfa Aesar 99.95%). Bi and Pd were introduced in quartz ampoules and sealed at 140 mbar of He gas. Then, the ampoules were heated from room temperature to 900 °C in 3 h, maintained 24 h at this temperature, slowly cooled down to 490 °C in 96 h and finally cooled down to

*Corresponding author: hermann.suderow@uam.es

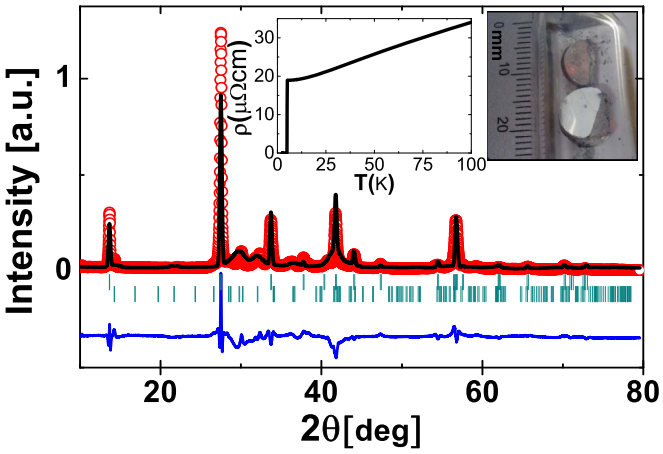

FIG. 1. (Color online) Powder diffraction pattern of β-Bi_2Pd. Red symbols are the experimental points. The black line is the best fit to β-Bi_2Pd diffraction pattern [36]. Residuals are given by the blue line. The two series (upper and lower) of vertical green strikes represent, respectively, the position in 2θ scale of the reflections from the β-Bi_2Pd ($I4/mmm$) and α-Bi_2Pd ($C12/m1$) phases. Insets show a photograph of one β-Bi_2Pd crystal and the temperature dependence of the resistivity.

395 °C in 200 h. This temperature is about 15 °C above the temperature for the formation of the α-Bi_2Pd phase [35]. To avoid formation of the α phase, we quenched the crystals down to ambient temperature by immersion in cold water. We obtained large crystals of 5 mm × 5 mm × 3 mm. To characterize them, we made x-ray diffraction on crystals milled down to powder (Fig. 1, using x rays with wavelength 1.54 Å). We find β-Bi_2Pd ($I4/mmm$, see Ref. [37]) with refined lattice parameters $a = b = 3.36(8)$ Å and $c = 12.97(2)$ Å and no trace of α-Bi_2Pd. We made in total twelve growths, varying slightly the conditions for the quench, growth temperature, and initial composition, and obtained always crystals with a resistivity versus temperature very similar to the one shown in Fig. 1. The temperature dependence of the resistivity is shown in the inset of Fig. 1. The superconducting transition in our sample of β-Bi_2Pd crystals occurs at 5 K. Previous resistivity measurements in this material reported a slightly higher value of T_c (around 0.3 K larger) and a residual resistivity three times smaller than the one found here [17]. The specific heat transition of our samples is sharp, of about 30 mK width [38], contrasting the transition width of about 300 mK reported in Ref. [17]. We measured also the upper critical field $H_{c2}(T)$ using the resistivity and susceptibility as a function of temperature or magnetic field for the field applied parallel to the c axis. The results coincide with the positions where we also observed vanishing superconducting features in STM tunneling conductance.

To make the STM measurements, we use a homebuilt setup installed in a dilution refrigerator with an energy resolution in the tunneling spectroscopy of 0.15 K. The construction is similar to Ref. [39]. We also took a few tunneling data at fields parallel to the surface using the three-axis coil system described in Ref. [40]. We use an Au tip cleaned by repeated indentation on an Au sample as described in Ref. [41]. We make the STM measurements in a sample roughly 1-mm thick, which was cleaved using a scotch tape at ambient conditions after gluing it using silver epoxy to the sample holder. Usually, the bias voltage is kept at 10 mV or below, and the tunneling conductance is of a few tenths of microsiemens. The topography and vortex lattice images are independent of the tunneling parameters. To obtain vortex lattice images, we cut the feedback loop at each point and make full I-V curves, as in previous work [42]. No filtering or image treatment is applied to the topography and the conductance maps shown here.

III. RESULTS

The tetragonal structure with Bi-Pd blocks (left panel of Fig. 2) suggests that it is easy to obtain clean and atomically flat surfaces by cleavage or exfoliation. In Fig. 2 (right panels),

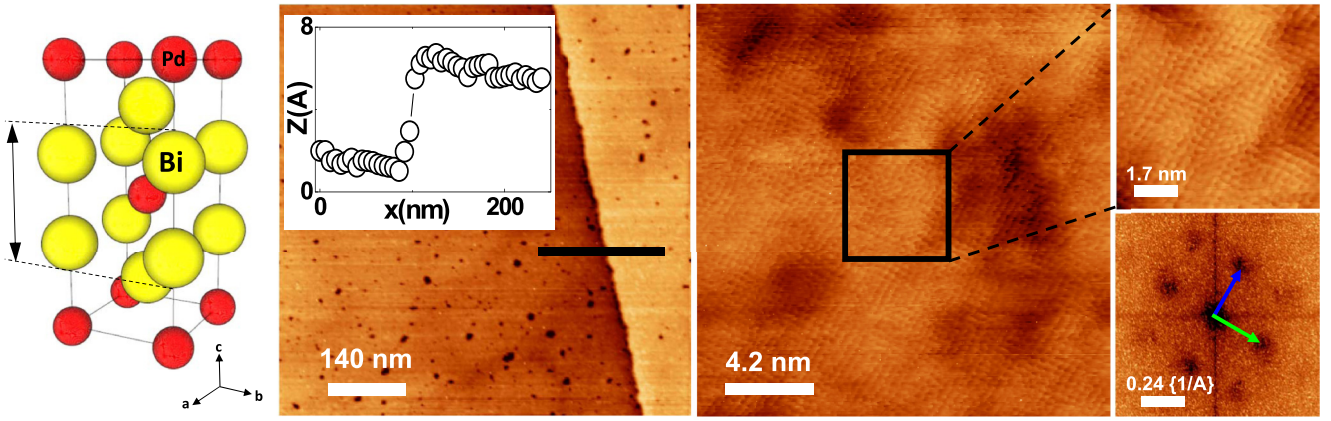

FIG. 2. (Color online) Imaging of the surface of β-Bi_2Pd at different length scales. Images are taken at a bias voltage of 10 mV and conductance 0.1 μS at 0.15 K. Lattice structure, highlighting the cleaving plane with distance between two successive planes $d = 6.5$ Å is shown in the left panel. The inset in the next panel from the left shows a cut through a line with a step edge whose size corresponds to the distance between cleaving planes. The corresponding distance is shown by an arrow in the left panel. The next panel shows an image with atomic resolution, giving the square atomic Bi lattice. The right panels show a zoom (top) and the Fourier transform (bottom). Blue and green arrows give crystalline axis.

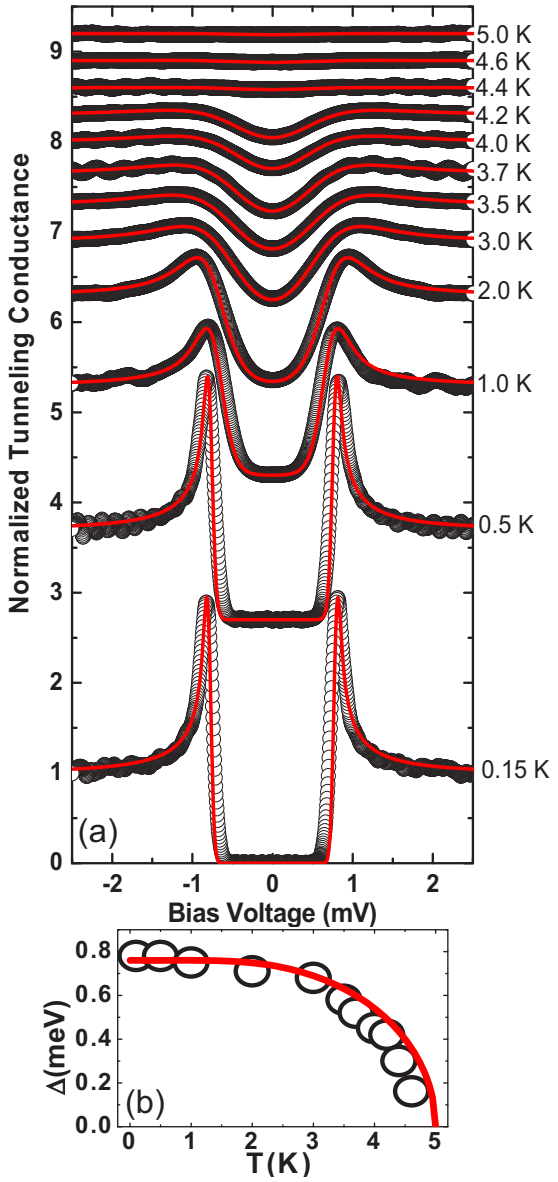

FIG. 3. (Color online) In (a), we show the temperature dependence of the experimental tunneling conductance (black dots). Red lines are fits to the s-wave BCS expression at each temperature. The values of Δ obtained are plotted in (b), together with the temperature dependence obtained from BCS theory (red line).

we show atomic resolution topography images taken on the surface of the sample at 0.15 K. We find indeed a square atomic lattice. The Fourier transform of the topography images gives a lattice parameter of $a = b = 3.3$ Å, coinciding with values found in x-ray experiments. Surfaces are atomically flat over hundreds of nanometers. Small step edges are sometimes viewed in the images. The step edge in Fig. 2 is of 6.5 Å height, which corresponds to the distance between adjacent Bi-Pd groups (black arrow in left panel of Fig. 2). Bi-Pd groups are more strongly coupled than the Bi-Bi sheets, because the directional Bi-Bi bonds are weaker than the Bi-Pd bonds [32]. Thus we conclude that the surfaces in Fig. 2 are made out of the square Bi lattice.

Figure 3 shows the tunneling conductance versus bias voltage as a function of temperature. At 0.15 K, we find clear superconducting quasiparticle peaks and no conductance at zero and low bias. We can fit our data using single-gap BCS theory and $\Delta = 0.76$ meV. We need to add small additional broadening, possibly due to the energy resolution of our setup, with a Gaussian distribution of width 30 μeV. The temperature dependence of the tunneling density of states can be fitted just by varying Δ with temperature and shows that superconductivity disappears at about 5 K and that the obtained $\Delta(T)$ follows well the single-gap BCS theory.

When we apply a magnetic field parallel to the c axis, we observe an ordered hexagonal vortex lattice on large atomically flat regions. In Fig. 4, we show vortex lattice images from 5 to 500 mT. A hexagonal Abrikosov lattice is observed in all images. The intervortex distance is modified as expected for the hexagonal vortex lattice $d_\Delta = 1.075\sqrt{\frac{\phi_0}{B}}$ (with ϕ_0 being the flux quantum).

We find no relation between the orientation of the vortex lattice with step edges or other defects in the sample. Instead, we find that the orientation of the vortex lattice is determined by the underlying crystalline lattice (arrows in Fig. 4). One of the three main vortex lattice directions is always parallel to one of the two crystalline axes. This gives two equivalent orientations for the hexagonal vortex lattice at any magnetic field.

Figure 5 shows that we can find two orientations of the vortex lattice in different locations of the sample at a fixed magnetic field. Thus the hexagonal vortex lattice is broken up into two domains each with one main axis of the vortex lattice oriented along one crystal axis.

The spatial dependence of the superconducting density of states in and around vortices shows that the gap fully closes inside the vortex core [Fig. 6(a)]. We do not observe signatures of Caroli-de Gennes-Matricon Andreev core states [43–45]. From the residual resistivity of our samples ($\rho = 18$ $\mu\Omega$ cm just above T_c), we estimate the mean free path using Drude formula and find $\ell = 15.3$ nm. On the other hand, the in-plane coherence length from the upper critical field [discussed below, $H_{c2}(T = 0\text{ K}) = \frac{\Phi_0}{2\pi\xi^2}$] yields $\xi = 23$ nm. Thus $\ell < \xi$ and Caroli-de Gennes-Matricon states are smeared by defect scattering [46].

In Fig. 6(b), we show the spatial dependence of the zero-bias conductance $\sigma_0(r)$ along a path crossing several vortex cores at 0.3 T in β-Bi_2Pd (blue points), and the expectation assuming vortex core overlap far from H_{c2}. The latter is calculated by summing over relevant neighbors (r_i) using $\sigma_0(r) = \sum_i 1 - \tanh((r_i - r)/\xi)$ (dark dashed line) with $\xi = 23$ nm. This approximation agrees with microscopic calculations showing that the intervortex density of states for single band superconductors in the dirty limit is practically negligible for fields below about half H_{c2} [47–49]. The magnetic field increase of the intervortex density of states is pronounced, as shown by the blue points in Fig. 6(c). These points are obtained from the magnetic field dependence of the tunneling conductance exactly in between three vortices (Fig. 7). It is smaller than the increase found in the superconductors 2H-$NbSe_2$, 2H-NbS_2 and MgB_2 [colored points in Fig. 6(c)] but also above the increase expected for a single-gap s-wave superconductor [dark dashed line in Fig. 6(c), obtained from

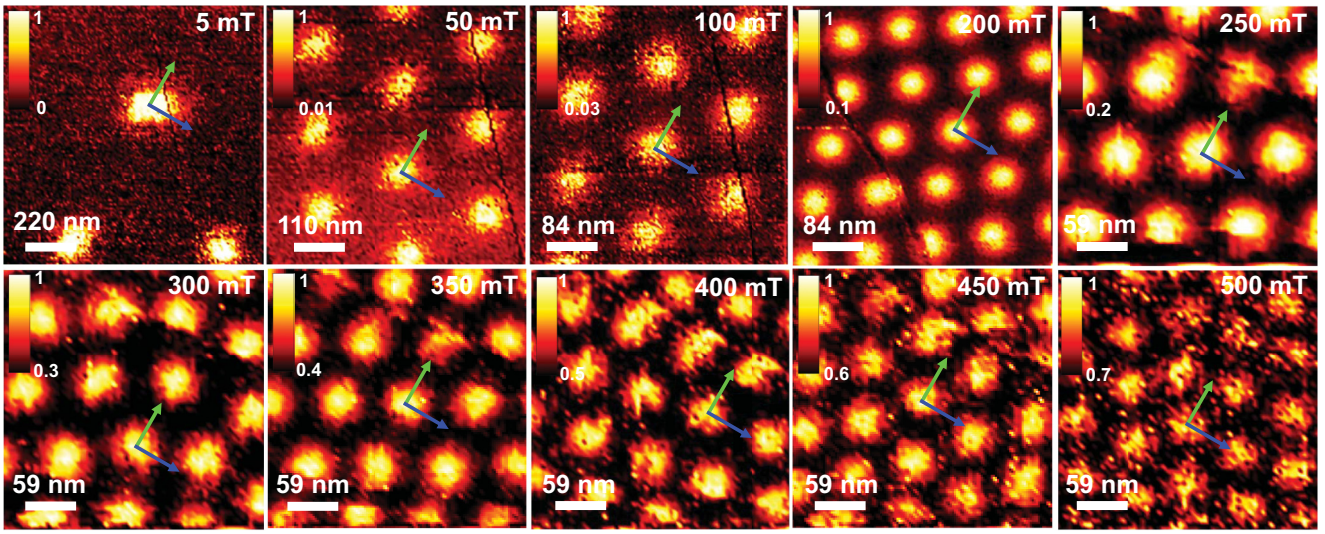

FIG. 4. (Color online) The vortex lattice as a function of the magnetic field applied parallel to the c axis in β-Bi_2Pd. The vortex lattice has a hexagonal symmetry for all values of the magnetic field. The images were taken at 150 mK and the magnetic field was increased up to $H_{c2} = 0.6$ T. Contrast in the zero-bias conductance is shown by the color scale. The crystalline orientation is shown as green and blue arrows in each panel.

the minima of $\sigma_0(r)$]. When we apply the magnetic field along the basal plane, we find a smaller sized intervortex density of states, closer to expectations for a single-gap s-wave superconductor [filled blue point in Fig. 6(c)]. Our data show that the tunneling conductance in-between vortices for the magnetic field applied along the c axis is more affected by the magnetic field than expectations for a single-gap superconductor.

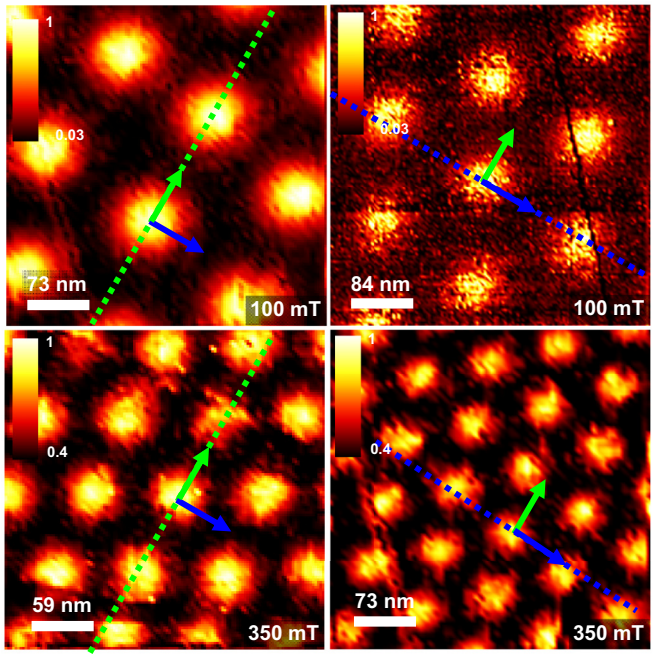

FIG. 5. (Color online) Vortex lattice at two different magnetic fields. In each magnetic field, we show two vortex images obtained at different scanning windows. Note the change in the orientation with respect to the atomic lattice, as marked by green and blue arrows. Contrast (zero-bias conductance) is shown with the color scales.

We have measured $H_{c2}(T)$ using resistivity and susceptibility (Fig. 8), and compared results with available data in a sample with a larger mean free path [17]. A smaller mean free path leads to a shorter coherence length and hence to an increased H_{c2}(T), also in multigap superconductors, see for instance MgB_2 [10,50–53]. Here, however, we do not observe such an increase in H_{c2} and instead we find slightly smaller $H_{c2}(T)$ than in previous measurements on samples with a larger mean free path.

To explain this result, we have calculated $H_{c2}(T)$ using a multiband approach and the method described in Refs. [15,16,18–20] (see also Appendix for details). We simplify the Fermi surface by using a two-band description, with differing Fermi velocities $v_{F,i}$, electron-phonon coupling λ_{ij} and electron scattering parameters $\tau_{i,j}$ (with subindices i, j for each band). We assume that the intraband and interband electron-phonon coupling constants λ_{ij} are connected together as $\lambda_{11} = \lambda_{21} = 1$ and $\lambda_{22} = \lambda_{12} = 0.3$. The superconducting gap has then the same value in both bands. This reproduces our zero-field tunneling spectroscopy result (Fig. 3). For the electronic specific heat coefficient we use $\gamma = 13$ mJ/K^{2}mol and derive the partial densities of states for each band from the anisotropy in the Fermi velocity. We also correlate the values of the $\tau_{i,j}$ with the experimental values of the resistivities. To this end, we assume that the conductivities of each band are equal $\rho_1 = \rho_2$ and we deduce the relaxation rate for each part of the Fermi surface using $\tau_i = \frac{\rho_i \gamma_i v_{Fi}^2}{V_{\rm mol}}$. Where $V_{\rm mol}$ is the molar volume, γ the Sommerfeld coefficient of the specific heat, and ρ the resistivity. Moreover, $\lambda_{12}/\lambda_{21}$ is given by the ratio of the density of states in both bands. Thus, taking $\gamma = 13$ mJ/K^{2}mol, we deduce γ_i from the choice of the $\lambda_{i,j}$. We also assumed that the relaxation rate is isotropic and that each τ_i is split into intraband and interband scattering, parametrized by an additional coefficient, α, such that $\tau_{11} = \alpha\tau_1$, $\tau_{12} = (1-\alpha)\tau_1$. The introduction of interband scattering $\tau_{12} \neq 0$ is needed to decrease the sensitivity of $H_{c2}(T)$ to the

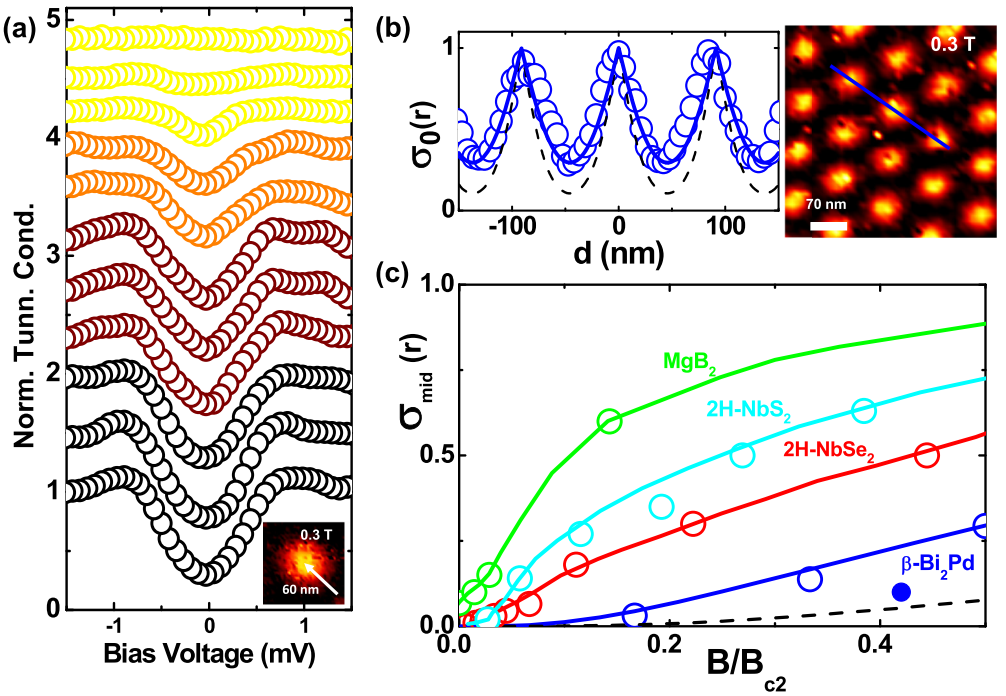

FIG. 6. (Color online) (a) The tunneling conductance vs bias voltage when entering a vortex core at 0.3 T along the path shown by the white arrow in the inset (one curve each 6 nm approximately). In (b), we show the normalized zero-bias conductance σ_0 as a function of the position at 150 mK and at $H/H_{c2} = 0.5$ (left panel, data shown as points, continuous blue line is a guide to the eye and black dashed line is calculated as discussed in the text). In (c), we show the magnetic field dependence of the zero-bias tunneling conductance $\sigma_{\rm mid}$ exactly in-between vortices (blue points, continuous blue line is a guide to the eye) when the field is applied along the c axis (open blue points) and when the field is applied along the plane (filled blue point). Data from 2H-$NbSe_2$, 2H-NbS_2 and MgB_2 (points, lines are guides to the eye) are from Refs. [12,13,42,43].

mean free path ℓ and obtain similar values of $H_{c2}(T)$ when ℓ is decreased. In Table I, we give the list of parameter values used to fit the two sets of data.

We neglect interband defect scattering for the data of Ref. [17]. This provides an excellent fit to the $H_{c2}(T)$ data of Ref. [17] (Fig. 8). If we simply decrease the mean free path to try to fit $H_{c2}(T)$ in our sample, we find an increase of the upper critical field. Only when allowing for interband scattering, with $\tau_{ij} \neq 0$ for $i, j \neq 0$, we find that $H_{c2}(T)$ does not increase when the mean free path is decreased. An intraband decrease of the mean free path invariably leads to a decreased coherence length and an increased upper critical field, but interband mixing can lead to similar values of the upper critical field. Introducing interband scattering, we obtain an excellent fit of our data, with an upper critical field that does not increase with decreased mean free path as shown by experiments (Fig. 8).

TABLE I. Parameters used to calculate the temperature dependence of the upper critical field along the c axis in the samples used in this work and in the samples of Ref. [17] (fits are shown as lines in Fig. 8, Fermi velocities are given in units of 10^6 m/s).

Sample	v_{F1}	v_{F2}	γ (mJ/K^{2}mol)	ρ ($\mu\Omega$ cm)	T_c (K)	α	β
This work	0.09	0.4	13	18	5.07	0.2	0.8
Ref. [17]	0.09	0.4	13	5	5.35	1	1

IV. DISCUSSION

The relationship between the symmetry and orientation of the vortex lattice with respect to the crystal lattice has been discussed in detail before. In 2H-$NbSe_2$, the vortex lattice is oriented parallel to the hexagonal crystal lattice [43,45]. In the nonmagnetic nickel borocarbide $LuNi_2B_2C$, when the magnetic field is applied along the c axis of the tetragonal crystal structure, the vortex lattice is square at high fields, with a side along [110] direction, in between [100] and [010] axes of the in-plane crystalline directions. The low-field hexagonal vortex phase preserves this orientation, showing two domains, each with the hexagonal vortex lattice oriented along one of the two [110] directions [13,54–57]. The interaction between crystal and vortex lattices is mediated by nonlocal effects, which introduce terms in the vortex-vortex interaction whose in-plane behavior depends on the shape of the Fermi surface [13,54–59]. In β-Bi_2Pd, the vortex lattice is hexagonal and oriented along the in-plane directions of the square crystal lattice [100] and [010]. This shows that the anisotropy of the Fermi surface and of the vortex-vortex interaction is also oriented along the same directions. Thus the anisotropy of the in-plane electronic properties, with the square fold Fermi surface, influences the vortex lattice orientation in β-Bi_2Pd.

The lack of increase of H_{c2} with mean free path shows on the other hand the influence of multiband effects on the mixed phase properties of β-Bi_2Pd. In MgB_2, two-dimensional sheets with strong electron-phonon coupling are derived from

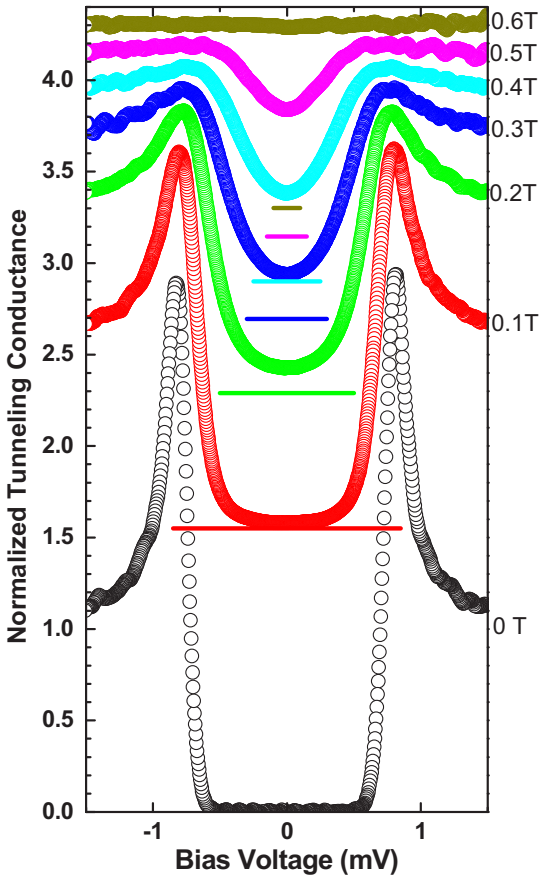

FIG. 7. (Color online) Magnetic field dependence of the full normalized tunneling conductance obtained exactly at the center between vortex cores. Magnetic field is applied along the c axis. Curves are shifted vertically for clarity. Lines provide the zero conductance value for each magnetic field.

the σ electrons of B orbitals, whereas the three-dimensional sheets are derived from π band orbitals. Interband scattering is particularly small in MgB_2. Previous theoretical work remarked that a decrease in H_{c2} might be observed by producing strong enough interband scattering [10,50]. The experiments show, however, a decrease of T_c with interband scattering, concomitant with a more isotropic superconducting gap and increased H_{c2} [51–53,60]. In β-Bi_2Pd, T_c is practically not modified by scattering and the gap is already nearly isotropic, but $H_{c2}(T)$ behavior shows the influence of multiband Fermi surface properties and interband scattering. β-Bi_2Pd has a Fermi surface with two nearly cylindrical sheets and two 3D sheets, derived from Pd $4d$ and Bi $6p$ states [31,32]. States from both Pd and Bi contribute to the density of states at the Fermi level, and in particular anisotropic $4d_{xy+yz}$ orbitals. Probably, the strong anisotropy of these orbitals favors interband scattering.

Let us compare the superconducting gap values and the vortex core overlap of β-Bi_2Pd with superconductors showing pronounced multigap behavior, MgB_2, 2H-$NbSe_2$, and 2H-NbS_2 [Table II and Fig. 6(c)] [12,13,18–20,42,43,60]. MgB_2 is the compound where the two gaps are more separated in energy, being the larger gap ($\Delta_>$) a factor of three higher than the smaller gap ($\Delta_<$) [60]. In 2H-NbS_2, the ratio between

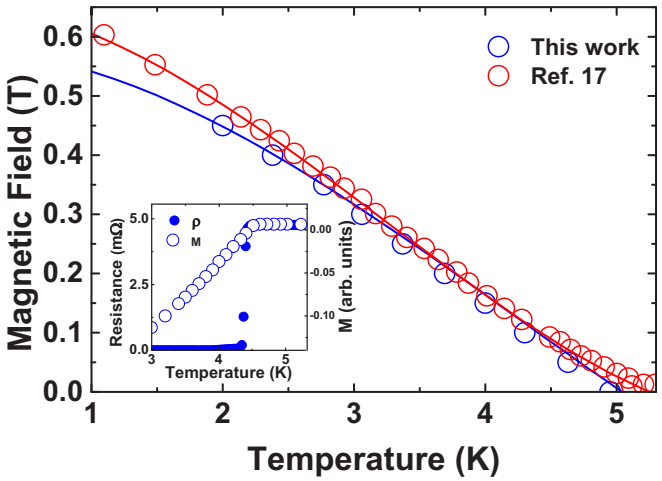

FIG. 8. (Color online) (a) $H_{c2}(T)$ along the c axis in our sample of β-Bi_2Pd with a residual resistivity of 18 $\mu\Omega$ cm (open blue points) and $H_{c2}(T)$ in sample of Ref. [17] with a residual resistivity of 5 $\mu\Omega$ cm (open red points). Lines are fits to each $H_{c2}(T)$ using the parameters explained in the text. Note that the upper critical field remains nearly the same, although the mean free path varies by a factor of four. Magnetic field is applied along the c axis. In the inset, we show the transition in resistance and susceptibility in our sample at a magnetic field of 0.1 T. The transitions remain sharp and well defined throughout the phase diagram.

the two gaps is somewhat smaller, around two [42]. The same gap ratio is found in 2H-$NbSe_2$, although in this material there is a sizable in-plane gap anisotropy with a wide distribution of gap values [43,61–63]. The vortex core overlap is smaller in 2H-$NbSe_2$ than in 2H-NbS_2 (Fig. 6). The anisotropy in the Fermi velocity is of the same order in 2H-$NbSe_2$ and 2H-NbS_2 than in MgB_2 [12,13,18–20,42,43]. Yet, the vortex core overlap is the highest in 2H-NbS_2, which has also more pronounced multigap properties. The strongest increase in vortex core overlap is thus produced by multigap superconductivity. In β-Bi_2Pd, the vortex core overlap is closest to a single isotropic superconducting gap, yet it lies sensibly above expectations. Thus the highly anisotropic Fermi surface produces a small but sizable effect on the intervortex electronic density of states.

We should note that the tunneling spectroscopy at the surface of all these materials is influenced by the quasi-2D nature of a large part of their Fermi surface, possibly favoring contributions from in-plane states [64]. As mentioned above, the Fermi surface of β-Bi_2Pd has a pronounced 3D character. This suggests that the interband scattering provides tunneling

TABLE II. Parameters used to account for $H_{c2}(T)$ of MgB_2, 2H-NbS_2, 2H-$NbSe_2$, and $\beta - Bi_2Pd$. The gap values $\Delta_>$ and $\Delta_<$ are obtained from Refs. [12,13,18–20,42,43,60].

	FS parameters from $H_{c2}(T)$		Δ (meV)	
	v_{F1} (10^6 m/s)	v_{F2} (10^6 m/s)	$\Delta_>$	$\Delta_<$
MgB_2	0.29	0.9	7.1	2.2
2H-NbS_2	0.155	3.1	0.97	0.53
2H-$NbSe_2$	0.055	1	1.2	0.75
β-Bi_2Pd	0.09	0.4	0.75	0.75

spectroscopy results in β-Bi_2Pd giving information about large parts of the Fermi surface, although this requires confirmation by detailed calculations of the tunneling conductance at the surface.

In conclusion, we have obtained atomically flat Bi surfaces in β-Bi_2Pd where we observe an isotropic superconducting gap and a hexagonal vortex lattice. By discussing tunneling spectroscopy, vortex lattice and $H_{c2}(T)$, we have shown that β-Bi_2Pd is a multiband superconductor with a single superconducting gap. Interband scattering precludes the usual increase of H_{c2} with a decreased mean free path. The hexagonal vortex lattice orientation locks to the crystalline lattice. We conclude that the mixed phase of superconductors is strongly modified in multiband Fermi surface materials, even when the zero-field superconducting tunneling conductance is not.

ACKNOWLEDGMENTS

We wish to acknowledge the support of Departamento Administrativo de Ciencia, Tecnología e Innovación, COLCIENCIAS (Colombia) Programa Doctorados en el Exterior Convocatoria 568-2012. This work was supported by the Spanish Ministerio de Economía y Competitividad (FIS2011-23488, MAT2011-27470-C02-02, and CSD2009-00013), by the Comunidad de Madrid through programs NANOFRONTMAG-CM (S2013/MIT-2850) and MAD2D-CM (S2013/MIT-3007) and by AXA Research Fund. We also acknowledge SEGAINVEX workshop of UAM, Banco Santander as well as PEOPLE, Graphene Flagship, and NMP programs of EU (Grant Agreements FP7-PEOPLE-2013-CIG 618321, 604391 and Nanopyme FP7-NMP-2012_SMALL-6 NMP3-SL 2012_310516). Furthermore, we acknowledge European Cooperation in Science and Technology MP1201 action, and discussions with P. Samuely. We are indebted with P. C. Canfield for setting up together with us our growth laboratory and teaching us details about crystal growth.

APPENDIX: CALCULATION OF THE UPPER CRITICAL FIELD

Several papers provide methods to calculate the upper critical field $H_{c2}(T)$ in multiband superconductors [10,15,16,18–20,50,53]. Here, we follow Ref. [16], a microscopic calculation of $H_{c2}(T)$ taking into account defect scattering. The upper critical field $H_{c2}(T)$ is found by calculating the set of β_i with the largest values that solve the following equations:

$$\varpi_i(n) = \omega_n + \pi T \sum_{j,m} (\lambda_{i,j}(m-n) + \delta_{mn}(\tau_{i,j}/2\pi T))\mathrm{sgn}(w_m), \tag{A1}$$

$$\Delta_i(n) = \pi T \sum_{j,m} [\lambda_{i,j}(m-n) - \mu^* \delta_{ij}\theta(\omega_c - |\omega_m|) + \delta_{mn}(\tau_{i,j}/2\pi T)]\mathcal{X}_j(m)\Delta_j(m), \tag{A2}$$

$$\mathcal{X}_i(n) = (2/\sqrt{\beta_i}) \int_0^\infty dq e^{-q^2} tan^{-1} \times \left(q\sqrt{\beta_i}/(|\varpi_i(n)| + \frac{ig}{2}\mu_B H_{c2}\mathrm{sgn}(\omega_n) \right), \tag{A3}$$

$$\beta_i = \frac{e}{2} H_{c2} v_{Fi}^2, \tag{A4}$$

$$\lambda_{i,j}(n) = \int_0^\infty d\omega \omega \alpha_{i,j}^2 \frac{F(\omega)}{\omega^2 + \omega_n^2}. \tag{A5}$$

Here, ω_n are the Matsubara frequencies, $\omega\alpha_{i,j}^2 F(\omega)$ is the electron-phonon coupling, Δ_i the Cooper pair wave function, $\tau_{i,j}$ the relaxation rate, $\lambda_{i,j}$ the electron-phonon coupling constant, and $v_{F,i}$ the Fermi velocity at a plane perpendicular to the magnetic field in each band i. The Fermi velocities discussed here are unrenormalized, i.e., as obtained without the pairing interactions. Their values eventually found in experiments (as quantum oscillation or photoemission) need to be renormalized by the electron-phonon interaction $\lambda_{i,j}$.

We see that the relevant parameters to describe mixture between different bands are the off-diagonal terms of matrices $\lambda_{i,j}$ and $\tau_{i,j}$. The superconducting order parameter is found by an equation of the same form of the BCS self-consistency gap equation (2). The first term of the equation between square brackets [ ] accounts for intraband and interband scattering due to electron-phonon interaction and defect scattering.

The bare Fermi velocity $v_{F,i}$ enters into the equation through the term $\mathcal{X}_j$, which also depends on the electron-phonon coupling and the interband and intraband scattering parameters $\lambda_{i,j}$ and $\tau_{i,j}$ through Eq. (1).

[1] B. Matthias, T. Geballe, and V. Compton, Superconductivity, Rev. Mod. Phys. **35**, 1 (1963).

[2] A. Y. Liu, I. I. Mazin, and J. Kortus, Beyond Eliashberg Superconductivity in MgB_2: Anharmonicity, Two-Phonon Scattering, and Multiple Gaps, Phys. Rev. Lett. **87**, 087005 (2001).

[3] G. Rubio-Bollinger, H. Suderow, and S. Vieira, Tunneling Spectroscopy in Small Grains of Superconducting MgB_2, Phys. Rev. Lett. **86**, 5582 (2001).

[4] E. Bascones and F. Guinea, Surface effects in two-band superconductors: Application to MgB_2, Phys. Rev. B **64**, 214508 (2001).

[5] F. Giubileo, D. Roditchev, W. Sacks, R. Lamy, D. X. Thanh, J. Klein, S. Miraglia, D. Fruchart, J. Marcus, and Ph. Monod, Two-Gap State Density in MgB_2: A True Bulk Property or a Proximity Effect? Phys. Rev. Lett. **87**, 177008 (2001).

[6] P. Szabó, P. Samuely, J. Kačmarčík, T. Klein, J. Marcus, D. Fruchart, S. Miraglia, C. Marcenat, and A. G. M. Jansen, Evidence for Two Superconducting Energy Gaps in MgB_2 by Point-Contact Spectroscopy, Phys. Rev. Lett. **87**, 137005 (2001).

[7] M. Iavarone, G. Karapetrov, A. E. Koshelev, W. K. Kwok, G. W. Crabtree, D. G. Hinks, W. N. Kang, E.-M. Choi, H. J. Kim, H.-J. Kim, and S. I. Lee, Two-Band Superconductivity in MgB_2, Phys. Rev. Lett. **89**, 187002 (2002).

[8] M. Zehetmayer, A review of two-band superconductivity: Materials and effects on the thermodynamic and reversible mixed-state properties, Superc. Sci. and Tech. **26**, 43001 (2013).

[9] P. Hohenberg and W. Werthammer, Anisotropy and temperature dependence of the upper critical field of Type-II superconductors, Phys. Rev. **153**, 493 (1967).

[10] A. Gurevich, Limits of the upper critical field in dirty two-gap superconductors, Physica C **456**, 160 (2007).

[11] P. Hirschfeld, M. Korshunov, and I. Mazin, Gap symmetry and structure of Fe-based superconductors, Rep. Prof. Phys. **74**, 124508 (2011).

[12] M. R. Eskildsen, M. Kugler, S. Tanaka, J. Jun, S. M. Kazakov, J. Karpinski, and O. Fischer, Vortex Imaging in the Π Band of Magnesium Diboride, Phys. Rev. Lett. **89**, 187003 (2002).

[13] M. R. Eskildsen, N. Jenkins, G. Levy, M. Kugler, O. Fischer, J. Jun, S. M. Kazakov, and J. Karpinski, Vortex imaging in magnesium diboride with $H \perp c$, Phys. Rev. B **68**, 100508 (2003).

[14] A. Kohen, T. Cren, T. Proslier, Y. Noat, W. Sacks, D. Roditchev, F. Giubileo, F. Bobba, A. Cucolo, N. Zhigadlo *et al.*, Superconducting vortex profile from fixed point measurements the "Lazy Fisherman" tunneling microscopy method, Appl. Phys. Lett. **86**, 212503 (2005).

[15] N. R. Werthamer, E. Helfand, and P. C. Hohenberg, Temperature and purity dependence of the superconducting critical field, H_{c2}, Phys. Rev. **147**, 288 (1966).

[16] S. V. Shulga, S.-L. Drechsler, G. Fuchs, K. H. Müller, K. Winzer, M. Heinecke, and K. Krug, Upper Critical Field Peculiarities of Superconducting YNi_2B_2C and $LuNi_2B_2C$, Phys. Rev. Lett. **80**, 1730 (1998).

[17] Y. Imai, F. Nabeshima, T. Yoshinaka, K. Miyatani, R. Kondo, S. Komiya, I. Tsukada, and A. Maeda, Superconductivity at 5.4 K in β-Bi_2Pd, J. Phys. Soc. Jpn. **81**, 113708 (2012).

[18] H. Suderow, V. G. Tissen, J. P. Brison, J. L. Martínez, S. Vieira, P. Lejay, S. Lee, and S. Tajima, Pressure dependence of the upper critical field of MgB_2 and of YNi_2B_2C, Phys. Rev. B **70**, 134518 (2004).

[19] H. Suderow, V. G. Tissen, J. P. Brison, J. L. Martinez, and S. Vieira, Pressure Induced Effects on the Fermi Surface of Superconducting 2H−$NbSe_2$, Phys. Rev. Lett. **95**, 117006 (2005).

[20] V. G. Tissen, M. R. Osorio, J. P. Brison, N. M. Nemes, M. García-Hernández, L. Cario, P. Rodiére, S. Vieira, and H. Suderow, Pressure dependence of superconducting critical temperature and upper critical field of 2H-NbS_2, Phys. Rev. B **87**, 134502 (2013).

[21] D. Larbalestier *et al.*, High-T_c superconducting materials for electric power applications, Nature (London) **414**, 368 (2001).

[22] A. V. Sologubenko, J. Jun, S. M. Kazakov, J. Karpinski, and H. R. Ott, Thermal conductivity of single-crystalline MgB_2, Phys. Rev. B **66**, 014504 (2002).

[23] E. Bauer, Ch. Paul, St. Berger, S. Majumdar, H. Michor, M. Giovannini, A. Saccone, and A. Bianconi, Thermal conductivity of superconducting MgB_2, J. Phys.: Cond. Matt. **13**, L487 (2001).

[24] G. M. Schmiedeshoff, J. A. Detwiler, W. P. Beyermann, A. H. Lacerda, P. C. Canfield, and J. L. Smith, Critical fields and specific heat of $LuNi_2B_2C$, Phys. Rev. B **63**, 134519 (2001).

[25] D. Lipp, M. Schneider, A. Gladun, S. Drechsler, J. Freudenberger, G. Fuchs, N. Nenkov, K. Mulcer, T. Cichorek, and P. Gegenwart, Specific heat and disorder in the mixed state of non-magnetic borocarbides, Europhys. Lett. **59**, 633 (2002).

[26] F. Bouquet, Y. Wang, I. Sheikin, T. Plackowski, A. Junod, S. Lee, and S. Tajima, Specific Heat of Single Crystal MgB_2: A Two-Band Superconductor with Two Different Anisotropies, Phys. Rev. Lett. **89**, 257001 (2002).

[27] J. Kačmarčík, Z. Pribulová, C. Marcenat, T. Klein, P. Rodiére, L. Cario, and P. Samuely, Specific heat measurements of a superconducting NbS_2 single crystal in an external magnetic field: Energy gap structure, Phys. Rev. B **82**, 014518 (2010).

[28] G. Seyfarth, J. P. Brison, M.A. Measson, J. Flouquet, K. Izawa, Y. Matsuda, H. Sugawara, and H. Sato, Multiband Superconductivity in the Heavy Fermion Compound $PrOs_4Sb_{12}$, Phys. Rev. Lett. **95**, 107004 (2005).

[29] G. Seyfarth, J. P. Brison, M.-A. Méasson, D. Braithwaite, G. Lapertot, and J. Flouquet, Superconducting $PrOs_4Sb_{12}$: A Thermal Conductivity Study, Phys. Rev. Lett. **97**, 236403 (2006).

[30] N. E. Alekseevski, N. N. Zhuravlev, and I. I. Lifanov, Zh. Eksp. Teor. Fiz. **27**, 125 (1954).

[31] M. Sakano *et al.*, Topologically protected surface states in a centrosymmetric superconductor β-$PdBi_2$, arXiv:1505.07231.

[32] I. R. Shein and A. L. Ivanovskii, Electronic band structure and Fermi surface of tetragonal low-temperature superconductor Bi_2Pd as predicted from first principles, J. Supercond. Novel Magnet. **26**, 1 (2013).

[33] P. C. Canfield and Z. Fisk, Growth of single crystals from metallic fluxes, Phil. Mag. B **65**, 1117 (1992).

[34] P. C. Canfield, *Solution Growth of Intermetallic Single Crystals: A Beginner's Guide* (World Scientific, Singapore, 2009), Chap. 2, pp. 93–112.

[35] H. Okamoto, The Bi-Pd (Bismuth-Palladium) system, J. Phase Equilibria **15**, 191 (1994).

[36] J. Rodríguez-Carvajal, Recent advances in magnetic structure determination by neutron powder diffraction, Physica B **192**, 55 (1993).

[37] N. N. Zhuravlev, Zh. Eksp. Teor. Fiz. **32**, 1305 (1957) [Sov. Phys. JETP, **5**, 1064 (1957)].

[38] J. Kacmarcik *et al.* (unpublished).

[39] H. Suderow, I. Guillamon, and S. Vieira, Compact very low temperature scanning tunneling microscope with mechanically driven horizontal linear positioning stage, Rev. Sci. Inst. **82**, 033711 (2011).

[40] J. A. Galvis *et al.*, Three axis vector magnet set-up for cryogenic scanning probe microscopy, Rev. Sci. Inst. **86**, 013706 (2015).

[41] J. G. Rodrigo, H. Suderow, S. Vieira, E. Bascones, and F. Guinea, Superconducting nanostructures fabricated with the scanning tunnelling microscope, J. Phys.: Condens. Matter **16**, 1151 (2004).

[42] I. Guillamón, H. Suderow, S. Vieira, L. Cario, P. Diener, and P. Rodiere, Superconducting Density of States and Vortex Cores of 2H-NbS_2, Phys. Rev. Lett. **101**, 166407 (2008).

[43] I. Guillamón, H. Suderow, F. Guinea, and S. Vieira, Intrinsic atomic-scale modulations of the superconducting gap of 2H−$NbSe_2$, Phys. Rev. B **77**, 134505 (2008).

[44] C. Caroli, P. G. de Gennes, and J. Matricon, Bound Fermion states on a vortex line in a type II superconductor, Phys. Lett. **9**, 307 (1964).

[45] H. F. Hess, R. B. Robinson, and J. V. Waszczak, Vortex-Core Structure Observed with a Scanning Tunneling Microscope, Phys. Rev. Lett. **64**, 2711 (1990).

[46] C. Renner, A. D. Kent, P. Niedermann, O. Fischer, and F. Levy, Scanning Tunneling Spectroscopy of a Vortex Core from the Clean to the Dirty Limit, Phys. Rev. Lett. **67**, 1650 (1991).

[47] A. A. Golubov and U. Hartmann, Electronic Structure of the Abrikosov Vortex Core in Arbitrary Magnetic Fields, Phys. Rev. Lett. **72**, 3602 (1994).

[48] A. E. Koshelev, A. A. Golubov, Mixed State of a Dirty Two-Band Superconductor: Application to MgB_2, Phys. Rev. Lett. **90**, 177002 (2003).

[49] T. Samuely, P. Szabo, Z. Pribulova, N. Sung, B. Cho, T. Klein, V. Cambel, J. Rodrigo, and P. Samuely, Type II superconductivity in $SrPd_2Ge_2$, Superc. Sci. Techn. **26**, 015010 (2013).

[50] A. Gurevich *et al.*, Very high upper critical fields in MgB_2 produced by selective tuning of impurity scattering, Superc. Sci. Tech. **17**, 278 (2004).

[51] S. L. Bud'ko and P. C. Canfield, Temperature-dependent H_{c2} anisotropy in MgB_2 as inferred from measurements on polycrystals, Phys. Rev. B **65**, 212501 (2002).

[52] M. Angst, S. L. Bud'ko, R. H. T. Wilke, and P. C. Canfield, Difference between Al and C doping in anisotropic upper critical field development in MgB_2, Phys. Rev. B **71**, 144512 (2005).

[53] M. Putti, V. Braccini, C. Ferdeghini, L. Pallechi, A. S. Siri, F. Gatti, P. Manfrinetti, and A. Palenzona, Critical field of MgB_2: Crossover from clean to dirty regimes, Phys. Rev. B **70**, 052509 (2004).

[54] M. R. Eskildsen, A. B. Abrahamsen, D. Lopez, P. L. Gammel, D. J. Bishop, N. H. Andersen, K. Mortensen, and P. C. Canfield, Flux Line Lattice Reorientation in the Borocarbide Superconductors with $H \| a$, Phys. Rev. Lett. **86**, 320 (2001).

[55] M. R. Eskildsen, A. B. Abrahamsen, V. G. Kogan, P. L. Gammel, K. Mortensen, N. H. Andersen, and P. C. Canfield, Temperature Dependence of the Flux Line Lattice Transition into Square Symmetry in Superconducting $LuNi_2B_2C$, Phys. Rev. Lett. **86**, 5148 (2001).

[56] L. DeBeer-Schmitt, M. R. Eskildsen, M. Ichioka, K. Machida, N. Jenkins, C. D. Dewhurst, A. B. Abrahamsen, S. L. Bud'ko, and P. C. Canfield, Pauli Paramagnetic Effects on Vortices in Superconducting $TmNi_2B_2C$, Phys. Rev. Lett. **99**, 167001 (2007).

[57] V. G. Kogan, M. Bullock, B. Harmon, P. Miranovic, L. Dobrosavljevic-Grujic, P. L. Gammel, and D. G. Bishop, Vortex lattice transitions in borocarbides, Phys. Rev. B. **55**, 8693(R) (1997).

[58] C. E. Sosolik, J. A. Stroscio, M. D. Stiles, E. W. Hudson, S. R. Blankenship, A. P. Fein, and R. J. Celotta, Real-space imaging of structural transitions in the vortex lattice of V_3Si, Phys. Rev. B **68**, 140503(R) (2003).

[59] I. Guillamon, M. Crespo, H. Suderow, S. Vieira, J. Brison, S. Bud'ko, and P. C. Canfield, Atomic resolution and vortex lattice studies of magnetic superconductors: A first approach in the nickel borocarbide $TmNi_2B_2C$, Physica C **470**, 771 (2010).

[60] P. Martínez-Samper, J. Rodrigo, G. Rubio-Bollinger, H. Suderow, S. Vieira, S. Lee, and S. Tajima, Scanning tunneling spectroscopy in MgB_2, Physica C **385**, 233 (2003).

[61] M. D. Johannes, I. I. Mazin, and C. A. Howells, Fermi-surface nesting and the origin of the charge-density wave in $NbSe_2$, Phys. Rev. B **73**, 205102 (2006).

[62] J. G. Rodrigo and S. Vieira, STM study of multiband superconductivity in $NbSe_2$ using a superconducting tip, Physica C **404**, 306 (2004).

[63] D. J. Rahn, S. Hellmann, M. Kalläne, C. Sohrt, T. K. Kim, L. Kipp, and K. Rossnagel, Gaps and kinks in the electronic structure of the superconductor 2H-$NbSe_2$ from angle-resolved photoemission at 1 K, Phys. Rev. B **85**, 224532 (2012).

[64] A. Kreisel, P. Choubey, T. Berlijn, W. Ku, B. M. Andersen, and P. J. Hirschfeld, Interpretation of Scanning Tunneling Quasiparticle Interference and Impurity States in Cuprates, Phys. Rev. Lett. **114**, 217002 (2015).